SEMARAK ILMU PUBLISHING

CFD Letters

Journal homepage:
https://semarakilmu.com.my/journals/index.php/CFD_Letters/index
ISSN: 2180-1363


# Numerical Study of Different Steady-State Flow Rigs for the Tumble Motion Characterization of a Four-Valve Cylinder Head

Andreas Theodorakakos[1,*]

[1] Laboratory of Thermo-Fluid Systems, Department of Mechanical Engineering, University of West Attica, Greece

**ARTICLE INFO**

***Article history:***
Received 7 March 2023
Received in revised form 5 April 2023
Accepted 6 May 2023
Available online 1 September 2023

***Keywords:***
Internal Combustion Engine; Tumble Ratio; Steady Flow Rig; CFD simulation

**ABSTRACT**

It is widely accepted that in-cylinder airflow structure strongly affects the performance and combustion of internal combustion (IC) engines. In order to enhance turbulence levels at the time of combustion, modern spark ignition engines (SI) usually employ a tumbling motion inside the cylinder. The tumble generated during the intake phase is mainly controlled by the cylinder head, inlet valves and ports configuration. The use of steady-state flow rigs is a common method to characterize the tumble generating ability of a given configuration. The purpose of this study is to perform CFD numerical simulations of two widely used tumbling measuring steady-state flow rig configurations, in order to compare and correlate the tumble ratios obtained from each one of them. A typical modern four-valve shallow pentroof cylinder head is considered and the flow is simulated for various inlet valve lifts. The results highlight the mass flow rate and tumble ratio differences between the two configurations.

## 1. Introduction

Alongside the continuous efforts for the electrification of vehicles, internal combustion (IC) engines are still improving, in terms of power density, efficiency and pollutant emissions. Moreover, the possible use of hydrogen [1-3], biofuels [4-6] or other $CO_2$ neutral fuels (synthetic fuels, also referred as e-fuels [7]) may prolong the existence of SI internal combustion engines in light duty vehicles. Reitz *et al.,* [8] provide a comprehensive summary about the future of IC engines, from the perspective of automotive engineers.

In-cylinder charge motion is one of the major factors that controls the combustion process in spark ignition (SI) engines [9] and the fuel-air mixing and combustion processes in compression ignition (CI) engines [10,11]. It also has a significant impact on engine heat transfer [12]. While in CI engines the preferred flow pattern is the swirling flow, modern SI engines use tumbling charge motion inside the cylinder. This tumbling motion increases the turbulence levels in the combustion chamber, and thus increases the burning speed and enhances the idle stability and the exhaust gas recirculation (EGR) susceptibility [13,14]. In modern gasoline direct injection (GDI) engines, the tumbling charge motion also controls the fuel mixing and stratification inside the cylinder [15,16].

* *Corresponding author.*
*E-mail address: atheod@uniwa.gr (Andreas Theodorakakos)*

https://doi.org/10.37934/cfdl.15.9.1831

The geometry of the cylinder head and inlet ports plays a key role in the charge motion inside the cylinder. The in-cylinder flow field can be experimentally measured in engines with optical access using appropriate laser diagnostics techniques, but this approach requires significant effort and expensive equipment. Although experiments with firing conditions are possible, due to the additional difficulties and restrictions imposed by combustion, it is more convenient to perform cold flow analysis under motoring conditions [17]. A more convenient method to characterize the tumble generating characteristics of a specific cylinder head geometry is the use of steady-state flow rigs. This approach has the additional advantage that it is relatively easy to study the flow in production engines cylinder heads. Such steady-state flow rigs can be used for in-cylinder velocity field PIV measurements [13,18,19] . More widely used are the "integral" steady-state methods, where tumble intensity is characterized by measuring the angular momentum flux, using an impulse torque meter or a paddle wheel [20-24]. Unfortunately, there is not any standardized and unique testing procedure for the quantification of the tumble intensity, so the existing methods provide results, which are not directly comparable. In that sense, the results obtained from these methods have rather a "relative" than an "absolute" validity. Xu [25] provided a complete overview of the main steady flow testing techniques for engine cylinder heads.

Beside experimental measurements, computational fluid dynamics (CFD) simulations have become a valuable and reliable tool for the analysis of the flow field inside the cylinder. Several studies comparing the experimentally measured flow field and tumble ratios with CFD obtained results, confirm the good agreement of the simulation results ([17,20,22,26-29]). CFD simulations can be effortlessly used to compare results for several different cylinder head arrangements, speeding up the process of manufacturing optimal designs. However, some related issues need special attention. The numerical grid, numerical methods and turbulence modelling used in the CFD simulations need careful selection. Moreover, if the tumble characteristics are of interest, there should be a known correlation between the tumble ratios obtained by the different steady-state flow bench configurations and the in-cylinder charge motion in motored (or firing) conditions.

The purpose of this study is to compare CFD results of the flow coefficient and tumble ratio, for a typical 4-valve cylinder head arrangement, mounted in two different steady-state flow rigs, using different numerical schemes, mesh densities and turbulence models, for various valve lifts.

## 2. Methodology

### *2.1 Tumble Measuring Flow Rig*

Steady-state flow rigs usually employ a paddle wheel measuring its rotational speed or an impulse swirl meter measuring the torque exerted by the flow. Due to problems related with mechanical issues and the flow disturbance caused by the paddle wheel, the use of an impulse swirl meter is considered more accurate. An impulse flow meter consists of a honeycomb flow straightener mounted in a distance from the cylinder head. These techniques, originally used for swirl measurements, have been extended to tumbling motion measurements, using the appropriate tumble adaptor. A widely used tumble adaptor, converting the tumbling charge motion into swirling motion, which is measured by an aforementioned device, is that used by Ricardo [30]. Two common configurations of this adaptor are used, the "T-type" and the "L-type" (Figure 1). In the "L-type" configuration, the flow is exiting in both direction of the adaptor tube and the geometry has a symmetry plane (for equal lift for the two inlet valves). The angular momentum is measured in one side of the tube, and is obviously half of the total angular momentum exiting the tube from both sides. In the "T-type" configuration, the tumble adapter tube is close in one side and the total mass flow is exiting through the impulse honeycomb swirl meter. The diameter of the tube ($D$) is

approximately equal to the bore (*B*). Typical lengths used for the tube (*L*) are in the range of 500mm. Because of angular momentum conservation, both those dimensions are not considered to be critical, although it should be noted that wall friction affects the results. The distance of the tube axis to the cylinder head (*H*), is a critical dimension affecting tumble. Ricardo uses a distance of *H=20mm+B/2*.

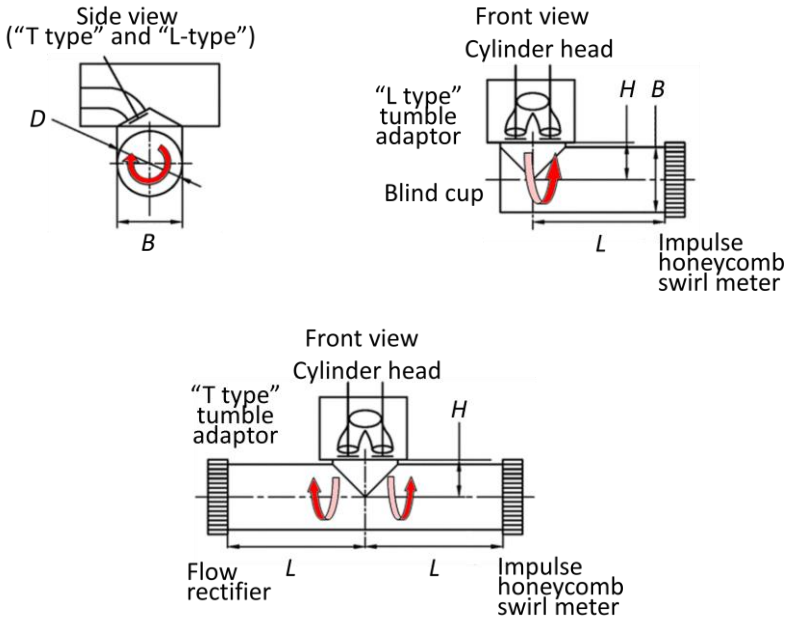


**Fig. 1.** "T-type" and "L-type" tumble adaptors

In steady-state state measurements, the flow through the test rig is created applying a constant pressure difference between inlet and outlet. This chosen pressure difference should ensure a fully turbulent flow, and is usually selected based on the Reynolds number, calculated using the intake valve inner seat diameter. For automotive sized cylinder head geometries, typical values used are in the range of 400-1000 mm $H_2O$.

According to the Ricardo method, the mass flow coefficients that can be calculated are the flow coefficient $C_f$ and the discharge coefficient $C_d$:

$$C_f = \frac{Q}{A_{in.seat} \cdot V_o} \qquad C_d = \frac{Q}{A_v \cdot V_o} \tag{1}$$

Concerning the tumble, the non-dimensional tumble number $N_{TR}$ can be calculated as ([21]):

$$N_{TR} = \frac{8G}{\dot{m} \cdot V_o \cdot B} \tag{2}$$

Where $Q$ is the air volume flow rate, $\dot{m}$ is the mass flow rate, $G$ is the torque measured by the impulse meter, $B$ is the cylinder bore diameter, $A_{in.seat}$ is the inner valve seat area, $A_v$ is the orifice area between valve head and valve seat area and $V_o$ is the velocity head $\left(\sqrt{2\Delta P/\rho}\right)$. In the case where only half of the total flow torque is measured (i.e. as in the "T-type" adaptor), only half of the total mass flow rate should be considered in the nominator of Eq. (2).

### *2.2 Geometry Modelling*

A parametric 3D solid model for the cylinder head, inlet valves and inlet port, was created using an appropriate CAD software (Figure 2). The design has straight inlet ports, shallow combustion chamber with small pentroof angle and medium sized squish zones, large intake valves and relatively large exhaust valves. The geometry closely resembles the configuration of an existing newly designed high power output SI engine.

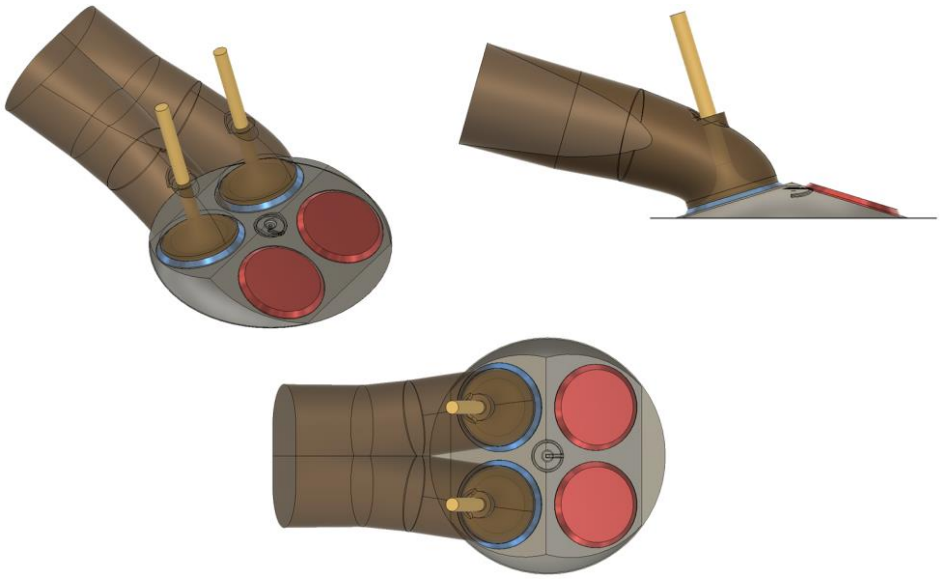

**Fig. 2.** Views of the 3D model of the simulated geometry

The main dimensions are shown in Table 1. The exhaust side was not modelled. For every simulated valve lift case, the valves were placed to the correct position.

**Table 1**
Main geometric dimensions of the simulated configuration

| | |
|---|---|
| Bore (mm) | 87.5 |
| Stroke (mm) | 89.7 |
| Inlet valves diameter (mm) | 32 |
| Valve's seat angle (deg) | 45$^o$ |
| Pentroof angle (deg) | 17$^o$ |

In order to accommodate the application of boundary conditions in the CFD simulation, an inlet plenum chamber upstream the inlet port and an outlet plenum chamber downstream the tumble measuring tube, were added. For the T-tube configuration, due to the existence of symmetry plane, only half of the complete geo. For both cases, the impulse honeycomb swirl meter that is used in the tumble adaptors, was not modeled metry is simulated. For both cases, the impulse honeycomb swirl meter that is used in the tumble adaptors, was not modeled by the numerical mesh. The torque that would be exerted by the flow to the swirl meter placed in a certain position along the exit tube is calculated from the angular momentum flux parallel to the tube's axis, relative to the center of the cross section, through the corresponded surface.

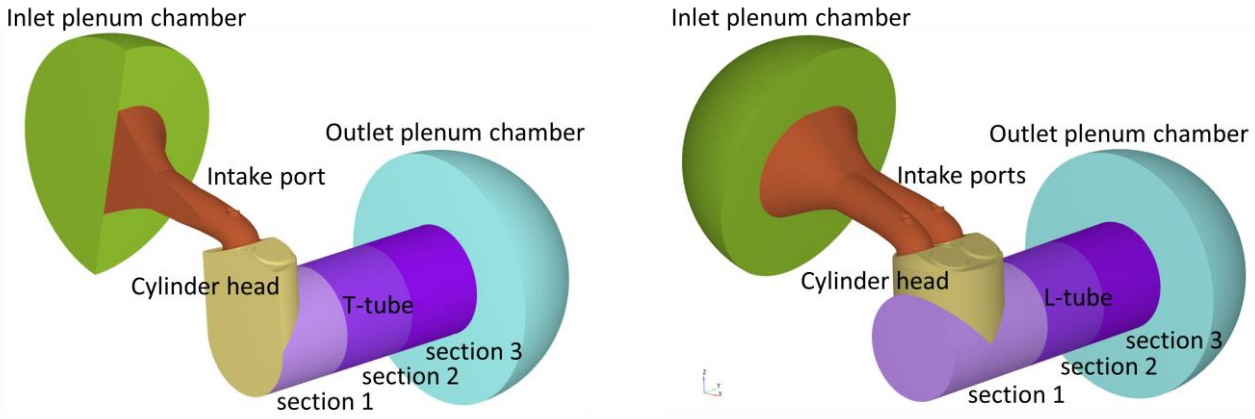


(a) (b)

**Fig. 3.** Computational domain for (a) T-tube, half model (b) L-tube

### *2.3 Meshing and CFD Simulation Procedure*

For this study the CONVERGE CFD software was used [31]. CONVERGE uses a fully autonomous meshing procedure, employing a cut-cell approach to create a body-fitted orthogonal numerical mesh. The geometry surface is immersed within a Cartesian block, and the software trims the cells at the intersecting surface. This initial Cartesian block is the "standard" density grid. Local grid refinements can be applied in any region of interest. Global grid refinement is also possible, and is actually utilized here in order to accelerate steady-state convergence.

The initial size of the "standard" density Cartesian grid in the x, y and z directions was 2 mm. Three successive levels of refinement were applied around the valve, the valve' seat and the spark plug (0.25 mm cell size). Two levels of refinement were applied near the walls of the inlet port and inside a cylindrical region near the valve opening (0.5mm cell size). One level of refinement was applied near the walls of the cylinder and the tube of the tumble rig (1 mm cell size).

Starting from the standard density grid, and successively coarsening or refining by a factor of 2, two more coarse grids (the "coarse" and the "very coarse"), and a finer grid ("fine") were constructed (Figure 4). Simulation results are reported and compared for the "coarse", the "standard" density and the "fine" grid. All simulations started from the very coarse mesh. When the monitored integral quantities (mass flowrate and angular momentum in the tube of the tumble rig) stop changing, within a loose tolerance limit, the solution proceeds to the next grid level. When the simulation has proceeded to the final grid level, steady state condition is assumed to be reached when the same integral quantities stop changing within a much stricter tolerance.

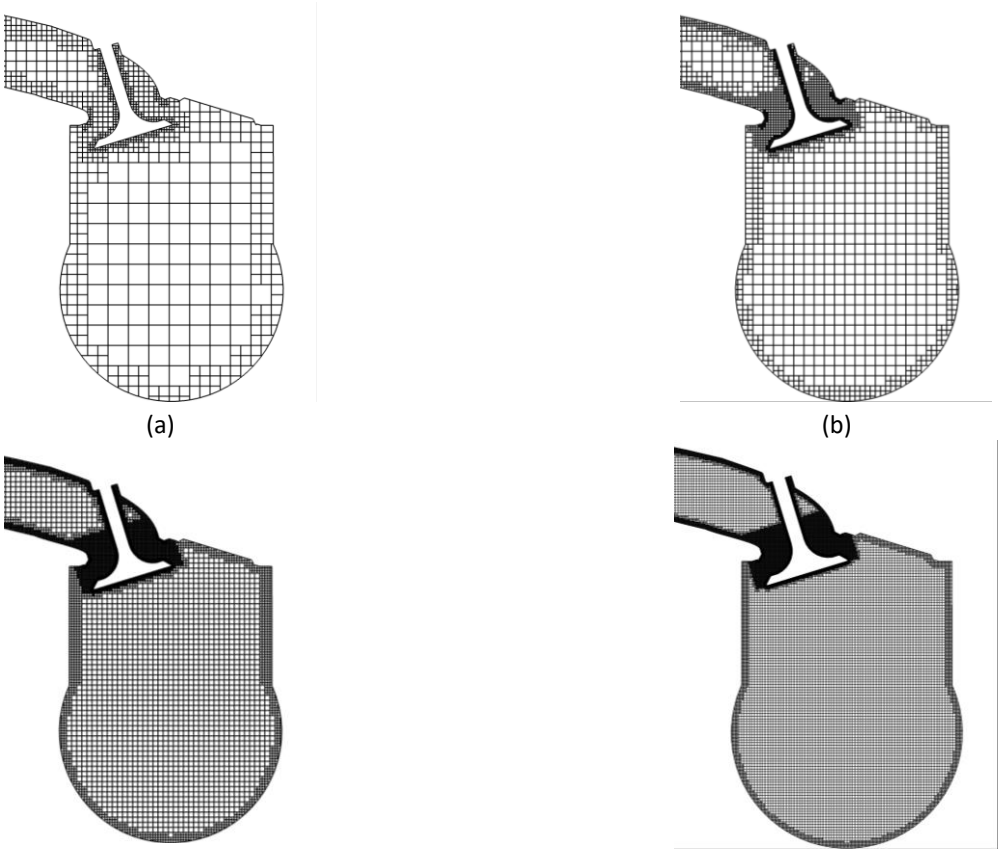


**Fig. 4.** Slice of the numerical mesh at the vertical plane through the axis of one of the inlet valves, for the T-tube rig case, (a) "very coarse" mesh (b) "coarse" mesh (c) "standard" density mesh (d) "fine" mesh

Table 2 summarizes the unrefined cell's edge length and the total cells in each of the meshes used in this study.

**Table 2**
Unrefined cell's edge length and the total number of cells in each of the meshes used (for 10 mm valve lift)

| Configuration | Grid | Unrefined cell's edge length (mm) | Total number of cells (In thousands, approx.) |
|---|---|---|---|
| T-tube (half geometry) | "Coarse" | 4 | 187 |
| | "Standard" | 2 | 1,266 |
| | "Fine" | 1 | 9,192 |
| L-tube | "Coarse" | 4 | 300 |
| | "Standard" | 2 | 2,031 |

### *2.4 Convective Schemes, Turbulence Models, Boundary Conditions*

The first configuration considered was the "T-tube" arrangement. This configuration was simulated for a medium valve lift (6 mm) using a combination of different grid resolutions, convective flux schemes and turbulence models. This step is necessary in order to arrive to an optimal set of models and parameters to be used for the following parametric simulations, so that the simulation results would be as accurate as possible, comparable to each other and requiring reasonable computational resources.

In this study the Reynolds-Average Navier-Stokes (RANS) approach was used and the turbulence models considered were the Standard RNG k-ε ([32]) and the k-ω SST model ([33]). Results were obtained and compared for the "coarse", the "standard" density and the "fine" grid.

The convective schemes considered were the First Order Upwind (FOU), and the MUSCL (Monotonic Upstream-Centered Scheme for Conservation Laws) scheme ([34]). In the FOU convective scheme, the velocities at the cell face between two adjacent cells are considered equal with the velocities of the upstream cell centre and it is thus first order accurate. MUSCL approximates the velocities at a cell face ($u_f$) using a linear reconstruction method. The method calculates two values for $u_f$ using a Taylor Series expansion from the centre of each of the two adjacent cells, to the face between them. By using a blending factor for those two reconstructed values, the scheme can vary between a second order upwind scheme (SOU) which uses only the reconstructed upwind velocities, and a reconstructed central difference discretization (CENTR) which uses the average of both the reconstructed upwind and downwind velocities, thus resulting a fourth order central discretization scheme. Both these schemes, the SOU and the reconstructed CENTR, were tested.

The pressure boundary condition set the outlet plenum chamber (hemispherical surface) was always set to 1 atm. The gauge pressure boundary condition set the inlet plenum chamber (hemispherical surface) was initially considered to be 600 mm $H_2O$, similar to that used in similar studies ([21]). Additional test was carried out using 400 mm $H_2O$ and 800 mm $H_2O$ inlet gauge pressure, in order to evaluate the influence of this parameter on the simulation results.

### *2.5 Calculation of the Rotating Flow Torque*

As already mentioned, the impulse honeycomb swirl meter that is used in the tumble adaptors, was not modeled by the numerical mesh The torque *G* that would be exerted to the swirl meter by the rotating flow in Eq. (2) is calculated from the angular momentum flux through the control surface $S_c$. The rate of change of angular momentum of a particle about a fixed point is equal to the torque applied to that particle:

$$\vec{T} = \frac{d\vec{L}}{dt} = \frac{d}{dt}(\vec{r} \times m\vec{u}) \tag{3}$$

Where $\vec{T}$ is the torque applied, $\vec{L}$ is the angular momentum, $m$ is the mass, $\vec{u}$ is the velocity and $\vec{r}$ is the position vector of the particle relative to the fixed point. The torque on a moving fluid material system occupying volume $V_s$ is:

$$\vec{T} = \frac{D}{Dt} \int\limits_{V_s(t)} \rho\vec{r} \times \vec{u}\, dV \tag{4}$$

Where $\rho$ is the density. Therefore, considering a fixed control volume $V$ inside a steady state flow field, the rate of change of the angular momentum of a material system is equal to the net outflow rate of the angular momentum through the surface enclosing this control volume:

$$\vec{T} = \frac{D}{Dt} \int\limits_{V_s(t)} \rho\vec{r} \times \vec{u}\, dV = \int\limits_{S(V)} (\rho\vec{r} \times \vec{u})\, (\vec{u} \cdot \vec{n}) dS \tag{5}$$

Where $S$ is the surface enclosing the fixed control volume $V$ and $\vec{n}$ the outward pointing normal unit vector of elemental surface $dS$. The control surface $S_c$ used for the calculation of the angular momentum flux was the circular cross-section interface between section 1 and section 2 of the numerical mesh, normal to the axis of the tube (Figure 4). The origin for the calculation of the angular momentum is the centre of the circular cross-section. The component of the torque vector that is of interest is the component $T_{axis}$ parallel to the axis of the tube. Assuming an infinitely thin control volume around surface $S_c$, the torque $T_{axis}$ that would need to be applied to the flow in order that the angular momentum parallel to the axis of the tube becomes zero at the exit of this thin control volume, is the opposite of the flux of this component of the angular momentum entering this volume through surface $S_c$.

$$T_{axis} = -\int_{S_c} (\rho r u_{circ})\, u_{axis} dS \tag{6}$$

Where $r$ is the distance of $dS$ from the center of the cross section, $u_{axis}$ is the velocity component parallel to the axis of the tube and normal to surface $S_c$ and $u_{circ}$ is the circumferential velocity component on surface $S_c$ around the center of the surface. The torque *G* in Eq. (2) is assumed to be equal with this torque $T_{axis}$.

## 3. Results

### *3.1 Initial Tests for the "T-tube" Configuration*

The "T-tube" configuration for 6 mm valve lift was simulated for all combinations of grids ("coarse", "standard" density and "fine"), convective schemes (FOU, SOU, CENTER and Blended MUSCLE with a blending factor of 0.5) and turbulence models (RNG k-ε and k-ω SST). For all cases, the standard upstream gauge pressure used was 600 mm $H_2O$. For 6 and 10 mm valve lifts, simulations were also carried out for 400 and 800 mm $H_2O$ upstream gauge pressure using "standard" density grid, FOU convective scheme and RNG k-ε turbulence model. The parameters compared are the flow coefficient $C_f$ (Eq. (1)) and the non-dimensional tumble number $N_{TR}$ (Eq. (2)).

#### *3.1.1 Effect of upstream gauge pressure*

Figure 5 shows the comparison of the predicted flow coefficient $C_f$ and the non-dimensional tumble number $N_{TR}$, for 10 mm valve lift using different upstream gauge pressures (400, 600 and 800 mm $H_2O$), for "standard" density grid, FOU convective scheme and RNG k-ε turbulence model. Although for increased upstream pressure there seems to be a slight increase for both parameters, differences are insignificant for $C_f$ and below 1% for $N_{TR}$. The same trends (with even lower variations) were predicted for 6 mm valve lift. These results indicate that for similar geometric dimensions a pressure difference in this range ensures a fully developed turbulent flow and justify the use of an upstream gauge pressure of 600 mm $H_2O$ in similar studies (i.e. [21]).

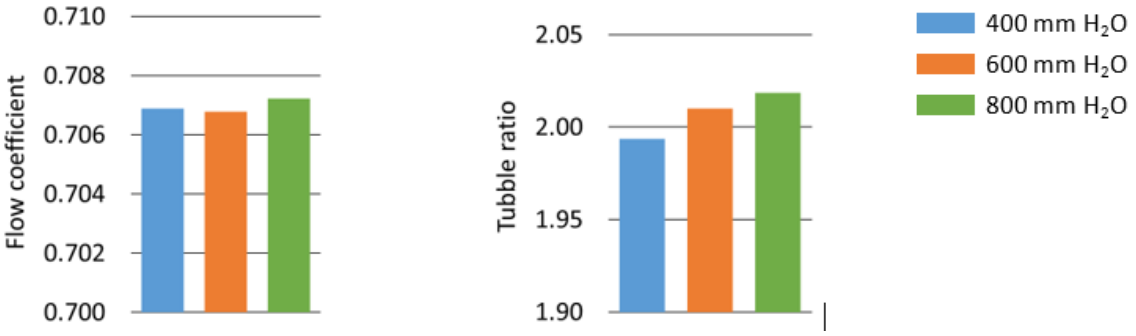


**Fig. 5.** Comparison of the predicted flow coefficient and the non-dimensional tumble number, for 10 mm valve lift using different upstream gauge pressures (400, 600 and 800 mm $H_2O$)

### *3.1.2 Effect of turbulence model*

The turbulence models considered were the two most widely used RANS models, the RNG k-ε ([32]) and the k-ω SST model ([33]). Figure 6 shows the comparison of the predicted flow coefficient $C_f$ and the non-dimensional tumble number $N_{TR}$, for 6 mm valve lift and different convective scheme, using "standard" density grid. For each convective scheme the use of RNG k-ε model seems to predict slightly higher flow coefficient (1 – 1.5%) and quite higher non-dimensional tumble number (9 – 11%), compared with the k-ω SST model. Those results are in line with observations in the literature that the RNG k-ε model produces lower turbulence levels and may underestimate the value of turbulent intensity, producing a less viscous flow (i.e. [35]). In theory, the RNG k-ε model should be more accurate in these kinds of flows.

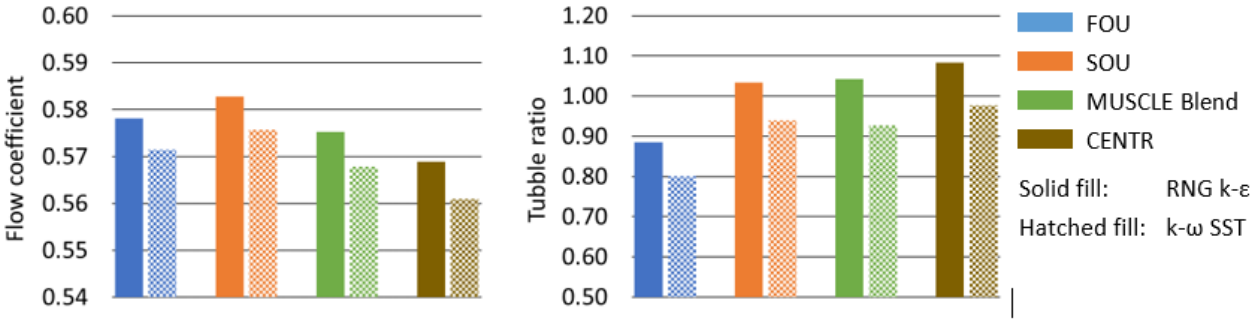


**Fig. 6.** Comparison of the predicted flow coefficient and the non-dimensional tumble number, for 6 mm valve lift using the RNG k-ε (solid fill bars) and the k-ω SST (hatched fill bars) turbulence models and different convective schemes

### *3.1.3 Effect of grid density and convective schemes*

Figure 7 shows the comparison of the predicted flow coefficient $C_f$ and the non-dimensional tumble number $N_{TR}$, for 6 mm valve lift using different grids ("coarse", "standard" density and "fine", Figure 4) and different convective schemes. The schemes used were the first order upwind (FOU), reconstructed second order upwind (SOU), reconstructed central scheme (CENTR) and MUSCLE blended scheme (blend of SOU and CENTR with 0.5 blending factor). The FOU scheme is first order accurate and thus of limited accuracy. Schemes that use downstream values (MUSCLE blended and CENTR) may lead to instabilities and convergence issues in flows of high Reynolds, as those under investigation. Overall, the most consistent results are obtained using the SOU scheme. The difference

of the results obtained with SOU, between the "standard" density and the "fine" grids are in the order of 3% for $C_f$ and 1% for the $N_{TR}$. Considering the above remarks, the following parametric simulations were carried out using the SOU scheme and the "standard" density grid, which is much more computationally economic compared with the "fine" grid.

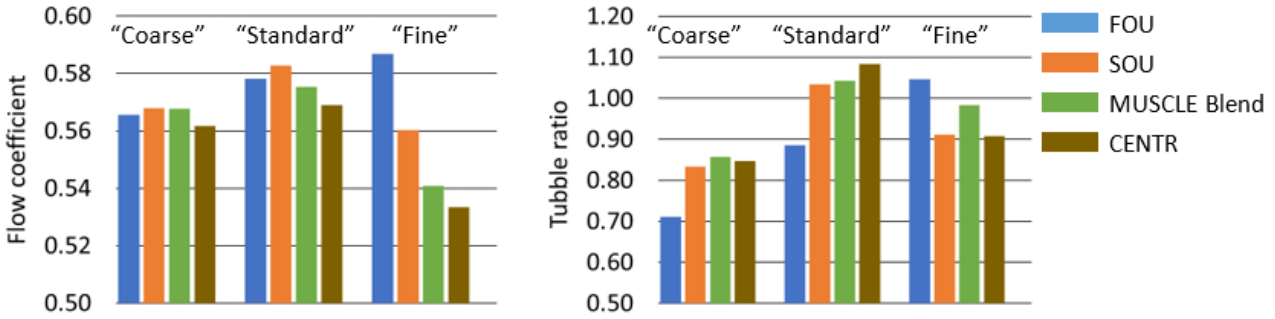


**Fig. 7.** Comparison of the predicted flow coefficient and the non-dimensional tumble number, for 6 mm valve lift using different grids ("coarse", "standard" density and "fine") and different convective schemes

### *3.2 Parametric Results for Valve Lift*

The "T-tube" and "L-tube" configurations were simulated for 2, 4, 6, 8 and 10 mm valve lifts. Figure 8 shows the comparison of the predicted flow coefficient $C_f$ and the non-dimensional tumble number $N_{TR}$ for the two configurations.

For valve lifts up to 6 mm, the flow coefficient is almost identical for the two configurations, showing an increase at a gradually declining rate. This is evidence that for low valve lifts the mass flow is mainly affected by the valve lift and not the downstream flow structure. For those valve lifts, the tumble number shows an increase at a gradually increasing rate. The tumble numbers predicted for the "T-tube" configuration are slightly higher.

For larger valve lifts, different behaviors are observed. The flow coefficient for the "T-tube" configuration continues to increase for up to 8 mm lift, but shows a decrease for 10 mm lift, indicating a decrease in the actual mass flow rate through the rig. For the "L-tube" the increase continues, but with significantly lower rate. For 8 mm valve lift, the tumble number predicted for the "L-tube" is higher than the "T-tube" configuration. This behavior although seems strange, it is consistent with the flow coefficient variations, as a higher tumble motion may cause a reduction in the mass flow. Those observations indicate that the flow coefficient for large valve lifts is mainly controlled by the flow structure inside the cylinder rather than the valve lift.

By inspecting Figure 8, it is evident that if the data for 8 mm valve lift were omitted, the curves for both the flow coefficient and the tumble number would be consistent for the two configurations. The flow coefficient would be almost identical (slightly lower for the "L-tube" at high lifts) and the tumble number slightly lower for the "T-tube" for the whole range of valve lifts. However, for 8 mm lift the two configurations show a different behavior. In order to eliminate the possibility for any kind of simulation error, those two cases were also simulated with different numerical meshes, convective schemes and turbulent models. In all those tests, this trend was always the same.

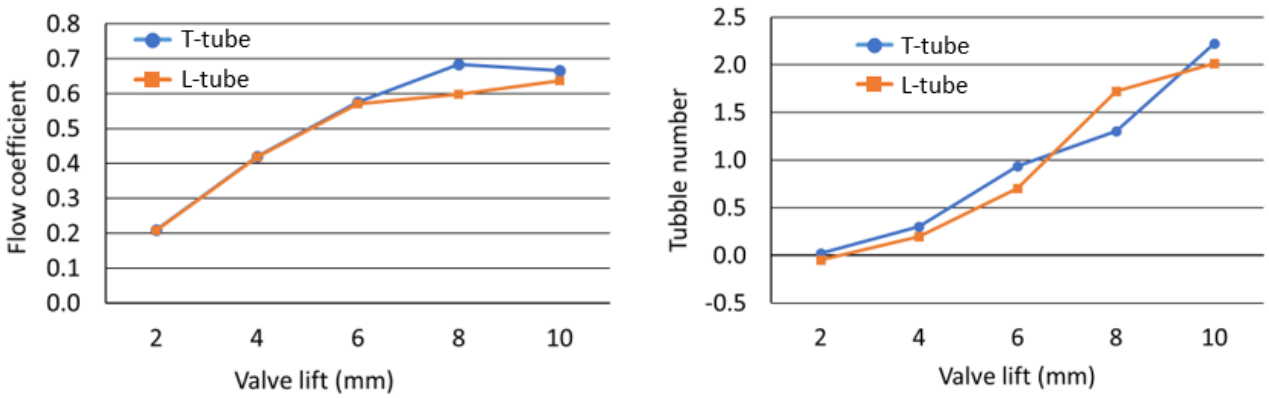


**Fig. 8.** Comparison of the predicted flow coefficient and the non-dimensional tumble number, for the "T-tube" and "L-tube" configurations, for various valve lifts

A closer inspection of the predicted flow field may provide some insight for this "anomaly". Figure 9 shows the flow field predicted for the two configurations, for 6, 8 and 10 mm valve lifts. It is evident that in the "L-tube" configuration, where the whole flow is headed towards the only side exit of the rig, the flow structure seems more organized, and the main vortices crated inside the cylinder occupies a larger region. In the "T-tube" configuration and for lower lifts, flow enters from the backside of the inlet valves with relatively high velocities, leading to the creation of a secondary counter rotating vortex beneath the inlet valves. For larger valve lifts (10 mm), that secondary vortex disappears, and the flow structure resembles that of the "L-tube". This change of the in-cylinder flow filed, from 8 mm to 10 mm valve lift leads to the reduction of the flow rate for the "T-tube" configuration. For 8 mm valve lift for the "L-tube" configuration, the stronger and well-organized vortex inside the cylinder leads to lower mass flow rate and increased tumble number.

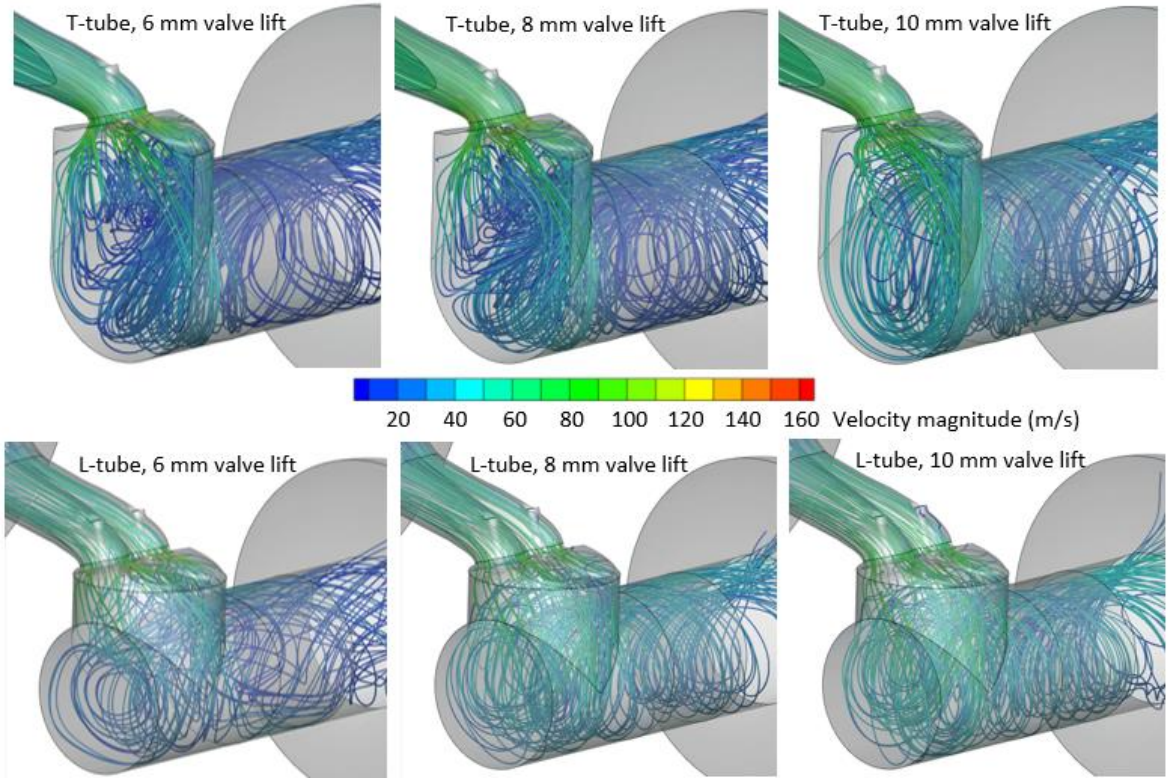


**Fig. 9.** Streamlines coloured by velocity magnitude, for the "T-tube" (upper row) and the "L-tube" (lower row) configurations, for 6 mm, 8 mm and 10 mm valve lift

## 4. Conclusions

CFD numerical simulations of the steady state flow through a modern SI engine cylinder head and two widely used tumbling measuring steady-state flow rig configurations were performed for various valve lifts. Several numerical meshes, convective schemes and turbulence models were tested in order to assess their influence on the flow coefficients and the tumble ratios.

Comparing the results obtained for the "T-tube" and the "L-tube" tumble measuring configurations, it is found that:

i. At low valve lifts, the mass flow is mainly affected by the valve lift, and the flow coefficients predicted for the two configurations are almost the same. For those lifts, the tumble ratios predicted for the "L-tube" configuration are slightly lower.
ii. At high valve lifts, the mass flow is mainly affected by the flow structure inside the cylinder. In the "L-tube" configuration, the flow inside the cylinder is dominated by a well-organized vortex. This is also the case for the "T-tube" configuration, but only for higher valve lifts. For this configuration at lower valve lifts, a counter rotating vortex inside the cylinder below the inlet valves is also present. The transition between those different flow patterns happens at mid to high valve lifts and affects both the mass flow rate and the tumble ratios.

A future study should compare and correlate the results obtained here, with numerical predictions concerning the tumble ratios inside the cylinder of a motoring engine.

**Acknowledgement**
The publication of this article was financially supported by the Special Accounts for Research Grants, University of West Attica. Convergent Science provided CONVERGE licenses and technical support for this work.

## References

[1] Shadidi, Behdad, Gholamhassan Najafi, and Talal Yusaf. "A review of hydrogen as a fuel in internal combustion engines." *Energies* 14, no. 19 (2021): 6209. https://doi.org/10.3390/en14196209
[2] Sementa, Paolo, Jácson Beltrão de Vargas Antolini, Cinzia Tornatore, Francesco Catapano, Bianca Maria Vaglieco, and José Javier López Sánchez. "Exploring the potentials of lean-burn hydrogen SI engine compared to methane operation." *International Journal of Hydrogen Energy* 47, no. 59 (2022): 25044-25056. https://doi.org/10.1016/j.ijhydene.2022.05.250
[3] Taib, Norhidayah Mat, Mohd Radzi Abu Mansor, and Wan Mohd Faizal Wan Mahmood. "Simulation of Hydrogen Fuel Combustion in Neon-oxygen Circulated Compression Ignition Engine." *Journal of Advanced Research in Numerical Heat Transfer* 3, no. 1 (2020): 25-36.
[4] Veza, Ibham, Mohd Farid Muhamad Said, Mohd Azman Abas, Zulkarnain Abdul Latiff, Mohd Rozi Mohd Perang, and Djati Wibowo Djamari. "Future Direction of Microalgae Biodiesel in Indonesia." *Journal of Advanced Research in Applied Sciences and Engineering Technology* 25, no. 1 (2021): 1-6. https://doi.org/10.37934/araset.25.1.16
[5] Gheidan, Abdelgader AS, Mazlan Abdul Wahid, Fudhail Abdul Munir, and Anthony Chukwunonso Opia. "Feasibility Study of Bio-fuel As a Sustainable Product of Biomass: An Overview of Its Fundamentals, Application and Environmental Impact." *Journal of Advanced Research in Fluid Mechanics and Thermal Sciences* 88, no. 2 (2021): 106-122. https://doi.org/10.37934/arfmts.88.2.106122
[6] Mohsin, R., Z. A. Majid, A. H. Shihnan, N. S. Nasri, Z. Sharer, and R. C. Mat. "Effects of Multi-Variant Biofuel on Engine Performance and Exhaust Emission of DDF Engine System." *Journal of Advanced Research in Fluid Mechanics and Thermal Sciences* 6, no. 1 (2015): 1-18.
[7] Wouters, Christian, Bastian Lehrheuer, Stefan Pischinger, Peter Seifert, Toni Raabe, Michael Kolbeck, Benjamin Rausch, Lars Menger, and André Casal Kulzer. "Evaluation of synthetic gasoline fuels and alcohol blends in a spark-

ignition engine." *SAE International Journal of Fuels and Lubricants* 15, no. 04-15-03-0017 (2022). https://doi.org/10.4271/04-15-03-0017
[8] Reitz, Rolf D., H. Ogawa, R. Payri, T. Fansler, S. Kokjohn, Y. Moriyoshi, A. K. Agarwal *et al.,* "IJER editorial: The future of the internal combustion engine." *International Journal of Engine Research* 21, no. 1 (2020): 3-10. https://doi.org/10.1177/1468087419877990
[9] Hill, P. G., and D. Zhang. "The effects of swirl and tumble on combustion in spark-ignition engines." *Progress in energy and combustion science* 20, no. 5 (1994): 373-429. https://doi.org/10.1016/0360-1285(94)90010-8
[10] Yoon, Sungjun, Seungpil Lee, Hyuckmo Kwon, Joonkyu Lee, and Sungwook Park. "Effects of the swirl ratio and injector hole number on the combustion and emission characteristics of a light duty diesel engine." *Applied Thermal Engineering* 142 (2018): 68-78. https://doi.org/10.1016/j.applthermaleng.2018.06.076
[11] Wang, Guixin, Wenbin Yu, Xiaobo Li, and Rui Yang. "Influence of fuel injection and intake port on combustion characteristics of controllable intake swirl diesel engine." *Fuel* 262 (2020): 116548. https://doi.org/10.1016/j.fuel.2019.116548
[12] Heywood, John B. *Internal combustion engine fundamentals*. McGraw-Hill Education, 2018.
[13] Kim, M. J., S. H. Lee, and W. T. Kim. "Correlation study of the measured tumble ratios using three different methods: Steady flow rig; 2-dimensional PIV; And 3-dimensional PTV water flow rig." *International journal of automotive technology* 7, no. 4 (2006): 441-448.
[14] Kaplan, Mahmut. "Influence of swirl, tumble and squish flows on combustion characteristics and emissions in internal combustion engine-review." *International Journal of Automotive Engineering and Technologies* 8, no. 2 (2019): 83-102. https://doi.org/10.18245/ijaet.558258
[15] Duronio, Francesco, Angelo De Vita, Luigi Allocca, and Michele Anatone. "Gasoline direct injection engines–A review of latest technologies and trends. Part 1: Spray breakup process." *Fuel* 265 (2020): 116948. https://doi.org/10.1016/j.fuel.2019.116948
[16] Saw, Om Prakash, Srinivasa Krishna Addepalli, and J. M. Mallikarjuna. *Effects of Cylinder Head Geometry on Mixture Stratification, Combustion and Emissions in a GDI Engine-A CFD Analysis*. No. 2019-01-0009. SAE Technical Paper, 2019. https://doi.org/10.4271/2019-01-0009
[17] Jamil, Abdullah, Masri B. Baharom, and A. Rashid A. Aziz. "IC engine in-cylinder cold-flow analysis–A critical review." *Alexandria Engineering Journal* 60, no. 3 (2021): 2921-2945. https://doi.org/10.1016/j.aej.2021.01.040
[18] El Adawy, Mohammed, M. R. Heikal, and A. Rashid A Aziz. "Experimental investigation of the in-cylinder tumble motion inside GDI cylinder at different planes under steady-state condition using stereoscopic-PIV." *Journal of Applied Fluid Mechanics* 12, no. 1 (2019): 41-49. https://doi.org/10.29252/jafm.75.253.28885
[19] El-Adawy, Mohammed, Morgan R. Heikal, A. Rashid A. Aziz, Muhammad I. Siddiqui, and Shahzad Munir. "Characterization of the inlet port flow under steady-state conditions using PIV and POD." *Energies* 10, no. 12 (2017): 1950. https://doi.org/10.3390/en10121950
[20] Mohammadebrahim, A., S. Kazemzadeh Hannani, and B. Shafii. "Investigation into the effect of intake port geometric parameters and blockage on flow coefficient and in-cylinder flow: Application to engine port design." *Scientia Iranica. Transaction B, Mechanical Engineering* 21, no. 2 (2014): 438.
[21] El-Adawy, Mohammed, M. R. Heikal, A. Rashid A. Aziz, M. I. Siddiqui, and Hasanain A. Abdul Wahhab. "Experimental study on an IC engine in-cylinder flow using different steady-state flow benches." *Alexandria Engineering Journal* 56, no. 4 (2017): 727-736. https://doi.org/10.1016/j.aej.2017.08.015
[22] Ramajo, D., A. Zanotti, and N. Nigro. "In-cylinder flow control in a four-valve spark ignition engine: numerical and experimental steady rig tests." *Proceedings of the Institution of Mechanical Engineers, Part D: Journal of Automobile Engineering* 225, no. 6 (2011): 813-828. https://doi.org/10.1177/0954407011400153
[23] Ramajo, Damian E., and Norberto M. Nigro. "In-cylinder flow computational fluid dynamics analysis of a four-valve spark ignition engine: comparison between steady and dynamic tests." *Journal of engineering for gas turbines and power* 132, no. 5 (2010). https://doi.org/10.1115/1.4000265
[24] Wahono, Bambang, Ardhika Setiawan, and Ocktaeck Lim. "Effect of the intake port flow direction on the stability and characteristics of the in-cylinder flow field of a small motorcycle engine." *Applied Energy* 288 (2021): 116659. https://doi.org/10.1016/j.apenergy.2021.116659
[25] Xu, Hongming. *Some critical technical issues on the steady flow testing of cylinder heads*. No. 2001-01-1308. SAE Technical Paper, 2001. https://doi.org/10.4271/2001-01-1308
[26] Harshavardhan, Ballapu, and J. M. Mallikarjuna. "Effect of piston shape on in-cylinder flows and air–fuel interaction in a direct injection spark ignition engine–A CFD analysis." *Energy* 81 (2015): 361-372. https://doi.org/10.1016/j.energy.2014.12.049
[27] Baratta, Mirko, Daniela Misul, Ezio Spessa, Ludovico Viglione, Giorgio Carpegna, and Francesco Perna. "Experimental and numerical approaches for the quantification of tumble intensity in high-performance SI

engines." *Energy Conversion and Management* 138 (2017): 435-451. https://doi.org/10.1016/j.enconman.2017.02.018

[28] Wahono, Bambang, Ardhika Setiawan, and Ocktaeck Lim. "Experimental study and numerical simulation on in-cylinder flow of small motorcycle engine." *Applied Energy* 255 (2019): 113863. https://doi.org/10.1016/j.apenergy.2019.113863

[29] Yang, Xiaofeng, Tang-Wei Kuo, Orgun Guralp, Ronald O. Grover Jr, and Paul Najt. "In-Cylinder Flow Correlations between steady flow bench and motored engine using computational fluid dynamics." *Journal of Engineering for Gas Turbines and Power* 139, no. 7 (2017): 072802. https://doi.org/10.1115/1.4035627

[30] Ricardo, J. "Steady state flowbench port performance measurement and analysis techniques." *Report DP93/0704* (1993).

[31] Richards, Keith J., Peter K. Senecal, and Eric Pomraning. "CONVERGE 3.0." *Convergent Science, Madison, WI* (2021).

[32] Yakhot, V. S. A. S. T. B. C. G., S. A. Orszag, Siva Thangam, T. B. Gatski, and CG1167781 Speziale. "Development of turbulence models for shear flows by a double expansion technique." *Physics of Fluids A: Fluid Dynamics* 4, no. 7 (1992): 1510-1520. https://doi.org/10.1063/1.858424

[33] Menter, Florianr. "Zonal two equation kw turbulence models for aerodynamic flows." In *23rd fluid dynamics, plasmadynamics, and lasers conference*, p. 2906. 1993. https://doi.org/10.2514/6.1993-2906

[34] Van Leer, Bram. "Towards the ultimate conservative difference scheme. V. A second-order sequel to Godunov's method." *Journal of computational Physics* 32, no. 1 (1979): 101-136. https://doi.org/10.1016/0021-9991(79)90145-1

[35] Shamami, K. Khademi, and M. Birouk. "Assessment of the performances of RANS models for simulating swirling flows in a can-combustor." *The Open Aerospace Engineering Journal* 1, no. 1 (2008). https://doi.org/10.2174/1874146000801010008